Electronic Supplementary Information

Noise suppression of 0D/2D flexible photodetectors mediated with atomically thin F-C functionalization on graphene channel

Po-Hsuan Hsiao[a], Kuan-Han Lin[a], Chian Hsieh[a], Le Vo Phuong Thuan[a], Ming-Fa Lin[b,d], and Chia-Yun Chen[a,c,d*]

[a]*Department of Materials Science and Engineering, National Cheng Kung University, Tainan 70101, Taiwan*
[b]*Department of Physics, National Cheng Kung University, Tainan 70101, Taiwan*
[c]*Program on Semiconductor Packaging and Testing, Academy of Innovative Semiconductor and Sustainable Manufacturing, National Cheng Kung University, Tainan 70101, Taiwan*
[d]*Hierarchical Green-Energy Materials (Hi-GEM) Research Center, National Cheng Kung University, Tainan 70101, Taiwan*

*Email: timcychen@mail.ncku.edu.tw

S1 Morphological observations of UV-absorptive CQD layers
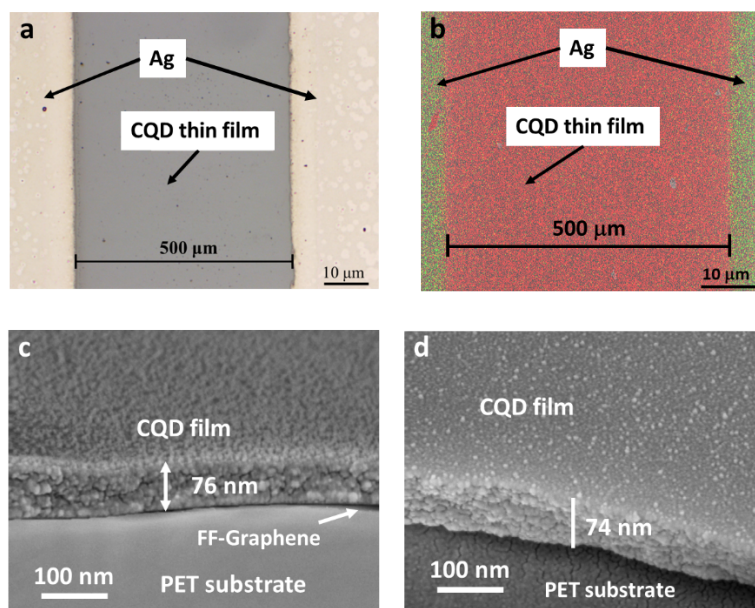**S1-1 Cross-sectional SEM images of heterostructures**

Fig. S1 (a) Top-view SEM image and (b) EDS mapping of CQD/FF-Gra/PET photodetector devices reveal a channel length of 500 μm between the silver electrodes. The cross-sectional SEM image of (c) CQD/FF-Gra/PET and (d) CQD/PET.

The CQD-based coupled heterostructures, including CQD/FF-Gra/PET and CQD/PET have been finely elaborated with large-area uniformity. Evidently, surfaces morphologies of these CQD-based configurations were characterized by cross-sectional SEM images, where the CQD layers were controlled with a fixed thickness of 75±1 nm. Both of as-prepared CQD/FF-Gra/PET and CQD/PET coupled heterostructures exhibited the uniform and finely stacked contact behaviors on monolayer FF-Gra or directly onto PET substrates, as evidenced in Fig. S1(c) and S1(d), respectively.

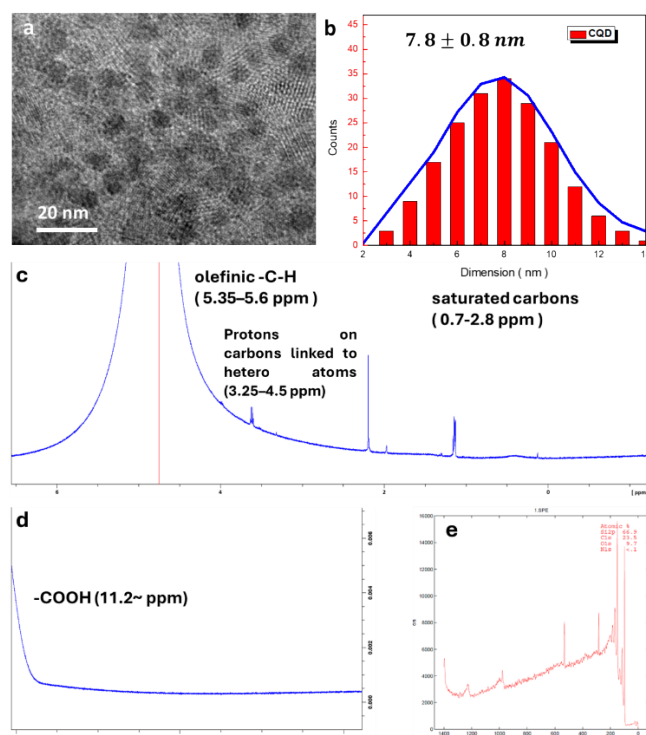**S1-2 Size distribution and   of synthetic monodispersed CQDs**

Fig. S2 (a) TEM image of densely accumulated monodispersed CQD structures, and the corresponding (b) size distribution analysis. The results show the high uniformity of monodispersed CQDs with average size of 7.8±0.8 nm. The molecular derivatives of as-synthesized CQD film were characterized with 1H-NMR spectra [Fig. S2(c) and S2(d)] and XPS full spectra [Fig. S2(e)].

Figs. S2(c) and S2 (d) display the characteristic proton signals of saturated carbons (0.7–2.8 ppm), with very low-intensity proton signals above ~1.8 ppm that may be originated from the aromatic portion and/or to the C-H resonances of saturated N/O β-carbons in heterocyclic compounds. Additionally, another low-intensity spectral feature appearing at 3.25–4.5 ppm corresponds to the signature of protons on carbons attached to heteroatoms. The two pronounced signals correspond to the existences of alkene -C-H (5.35–5.6 ppm) and -COOH around 11.2 ppm. Furthermore, the resonant features, normally located between ~6.7–8.5 ppm, corresponding to the signal of intermediate product such as aryl/aryl-fused 5/6-membered ring heterocycles (e.g., furan, pyrrole, and pyridine types), can not be observed in the present spectra.

In addition, the full XPS spectra of CQD films deposited on Si substrates are presented in Fig. S2(e). The results visualize the appearance of C, O and Si signals corresponding to the essential constitutes of CQDs, whereas the signals from other elemental compositions are extremely limited (<0.1%) based on the quantitative examinations. Taking the results from NMR and XPS analyses into consideration, it can be concluded that the existence of molecular derivatives, impurities and residual species from precursors are trivial as the synthesis of CQDs in this work is essentially based on high-purity glucose (99% in purity) as precursors, and thus the PL characteristics of CQD films are dominantly contributed from the functional features (-CO and -COOH mainly) at CQD surfaces, graphene core and the orbital hybridizations of outer/inner atomic configurations of CQD nanostructures, resulting in the generation of bound-carrier and free-carrier emissions from low-dimensional CQD nanostructures, which are in line with literature report (i.e., the difference in binding energy between

trion emission and exciton emission found in PL spectrum is 268 meV, which closely matches the results of carbon-based nanomaterials reported in the literature).

S2 Carrier density under various light-illumination conditions
S2-1 Mott Schottky results

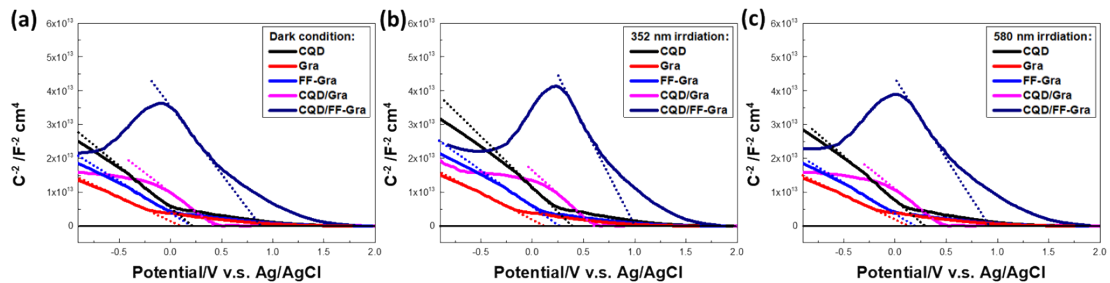
Fig. S3 Mott-Schottky plots of CQD/FF-Gra/PET devices under (a) dark condition, (b) 352-nm light irradiations and (c)580-nm light irradiations.

Charge carrier concentration and flat band potentials of CQD, Gra, FF-Gra, CQD/Gra and CQD/FF-Gra were calculated using the Mott-Schottky relation, given by Eq. (S1).[4]

$$\frac{1}{C^2} = \frac{2}{\epsilon_0 \epsilon_r A^2 e N_d}(V - V_{bi})$$

(S1)

where N_d, the charge carrier concentration, C the differential capacitance, ϵ_0 and ϵ_r the dielectric constants of vacuum and sample, respectively, A the electrode area, V and V_{bi} the applied potential and the built-in potential, respectively. According to Mott-Schottky plot, all the samples and their heterostructures investigated belonged to p type due to negative slope of C^{-2}-V curves. It is found that the carrier concentration at dark condition of CQD, Gra, FF-Gra, CQD/Gra and CQD/FF-Gra were estimated to be 2.82×10^{15} cm^{-3}, 9.32×10^{12} cm^{-3}, 3.18×10^{13} cm^{-3}, 3.72×10^{14} cm^{-3} and 7.55×10^{15} cm^{-3}, respectively. Under UV exposure (352 nm as light source), the carrier density was increased by an order of magnitude in dark condition in cases of CQD (4.51×10^{16} cm^{-3}), Gra (1.02×10^{13} cm^{-3}), FF-Gra (9.80×10^{13} cm^{-3}) and CQD/Gra (5.41×10^{15} cm^{-3}). It could be noted that the charge carrier concentration of CQD/FF-Gra (2.01×10^{18} cm^{-3}) under 352-nm light irradiation is three orders of magnitude higher than that in dark condition. Similarly, with visible-light irradiation (580 nm as light source) the carrier density ignorable change in CQD (6.51×10^{15} cm^{-3}), Gra (9.91×10^{12} cm^{-3}), FF-Gra (4.70×10^{13} cm^{-3}) and CQD/Gra (6.10×10^{14} cm^{-3}) cases.

S2-2 Hall-effect measurements

Hall effect measurements are conducted in vacuum, where the concentration and mobility of charge carriers in CQD, Gra, FF-Gra, CQD/Gra and CQD/FF-Gra at dark condition, 352 nm irradiation and 580 nm irradiation are estimated, as shown in Tables S1-S3, respectively.

Table S1 Hall effect measurement of CQD, Gra, FF-Gra, CQD/Gra and CQD/FF-Gra under dark condition.

Sample	Carrier concentration (cm^{-3})	Mobility (cm^2/Vs)

Sample	Carrier concentration (cm⁻³)	Mobility
CQD	2.8×10^{15}	23.7
Gra	9.28×10^{12}	51300
FF-Gra	3.1×10^{13}	6320
CQD/Gra	3.59×10^{14}	353
CQD/FF-Gra	7.62×10^{15}	798

Table S2 Hall effect measurement of CQD, Gra, FF-Gra, CQD/Gra and CQD/FF-Gra under 352-nm light irradiation.

Sample	Carrier concentration (cm⁻³)	Mobility (cm^2/Vs)
CQD	4.50×10^{16}	20.6
Gra	1.14×10^{13}	51300
FF-Grab	9.82×10^{13}	6201
CQD/Gra	5.41×10^{15}	321
CQD/FF-Gra	2.06×10^{18}	31988

Table S3 Hall effect measurement of CQD, Gra, FF-Gra, CQD/Gra and CQD/FF-Gra under 580-nm light irradiation.

Sample	Carrier concentration (cm⁻³)	Mobility (cm^2/Vs)
CQD	6.52×10^{15}	22.8
Gra	9.88×10^{12}	51300.0
FF-Gra	4.68×10^{13}	6230.0
CQD/Gra	6.04×10^{14}	326.0
CQD/FF-Gra	4.94×10^{16}	615.0

S3 Investigations of band diagrams
S3-1 Cyclic voltammetry measurement of monodispersed CQD layers
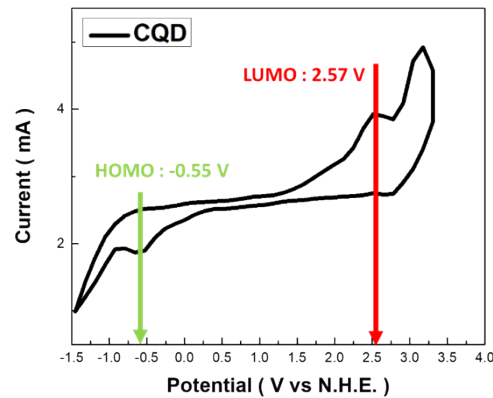

Fig. S4 CV measurement of monodispersed CQD layers.

Cyclic voltammetry measurements are utilized to directly determine the LUMO and HOMO energy levels of the CQD, respectively. Applying potentials above the LUMO to form an accumulation layer, or below the HOMO to form inversion layers, can lead to abrupt emergence of cathodic and anodic currents, respectively. Electrode for electrochemical analysis is prepared by drop-casting CQD suspensions (5 μl) and nafion (0.5 μl, 5% w) onto a glassy carbon electrode (diameter of 3 mm) and the results are presented in Fig. S4. The oxidation and reduction peaks related to electron and hole injections into the conduction and valence bands are consequently utilized to determine the E_{HOMO} and E_{LUMO} using the following three equations:[5]

$$E_{HOMO} = - e(E_{Ox.\ vs\ NHE} + 4.75)(eV) \tag{S2}$$

$$E_{LUMO} = - e(E_{Red.\ vs\ NHE} + 4.75)(eV) \tag{S3}$$

The reduction peak at −0.55 V and an oxidation peak at +2.57 V versus N.H.E are displayed. Accordingly, the values for E_{LUMO} and E_{HOMO} are calculated to be $E_{LUMO} = -2.23$ eV and $E_{HOMO} = -5.35$ eV, respectively.

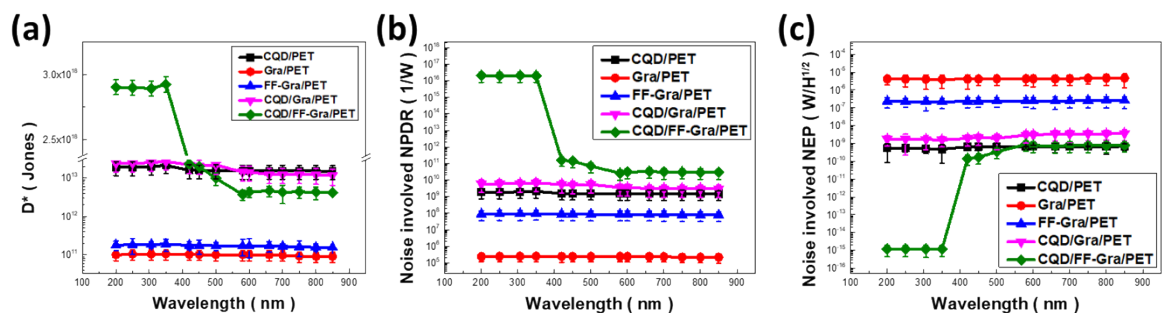## S4 Spectral detectivity, NPDR and NEP of CQD-based coupled heterostructures

Fig. S5 (a) Spectral dark-related detectivity (D*) as a function of irradiated wavelength: CQD/PET, Gra/PET, FF-Gra/PET, CQD/Gra/PET and CQD/FF-Gra/PET based devices, respectively. Plot of (b) modified normalized photocurrent to dark (noise) current ratio (NPDR) and (c) modified noise equivalent power (NEP) as a function of irradiated wavelength for various photodetectors, resepctively, where the noise features are employed for eavluating dark currents.

Detection detectivities (dark-current related detectivity (D*) and noise-involved detectivity (D_N) are both considered) are experimentally investigated, where the noise-

involved NPDR, termed as modified NPDR and noise-involved NEP, termed as modified NEP of CQD-based coupled heterostructures are presented as a function of light wavelengths, as shown in Fig. S4. Accordingly, The estimated D* values are 2.14×10^{13} Jones, 1.05×10^{11} Jones, 1.0×10^{11} Jones, 2.7×10^{13} Jones and 2.92×10^{18} Jones from CQD/PET, Gra/PET, FF-Gra/PET, CQD/Gra/PET and CQD/FF-Gra/PET based devices, respectively. The modified NPDR values considering noise features are 2.07×10^{9}, 2.5×10^{5}, 9.3×10^{7}, 6.65×10^{9} and 2.04×10^{16} W^{-1}, respectively, and the modified NEP values considering noise feature are 4.81×10^{-10}, 3.99×10^{-6}, 2.14×10^{-7}, 1.57×10^{-9} and 1.17×10^{-15} W/Hz$^{1/2}$, from CQD/PET, Gra/PET, FF-Gra/PET, CQD/Gra/PET and CQD/FF-Gra/PET based devices, respectively.

S5 Examinations of frequency-dependent noise and noise-related detectivity of CQD/FF-Gra hybrid structures

The noise patterns within low-frequency regime can be characterized with the involvment of 1/f noise, shot noise and thermal noise, respectively. The correlated expressions at frequency of 10 Hz are listed as below,

$$1/f \text{ noise} = \sqrt{I_{1/f}^2} = \sqrt{\frac{\alpha I_s^2}{fN}\Delta f} \tag{S4}$$

$$\text{Shot noise} = \sqrt{I_{sh}^2} = \sqrt{2qI\Delta f} \tag{S5}$$

$$\text{Thermal noise} = \sqrt{I_{th}^2} = \sqrt{\frac{4K_BT}{R_d}\Delta f} \tag{S6}$$

where α the Hooge experiential parameter in semiconductor with the value of 2×10^{-3}, I_s the net photocurrent, f the frequency, N the number of carriers, Δf the operating bandwidth of the photodetector, q the electron charge, I the mean current intensity, K_B the Boltzmann constant, T the measurement temperature and R_d the resistance. In addition, the formula of G-R noise is presented as below,

$$\text{G-R noise} = \sqrt{I_{GR}^2} = \sqrt{\frac{4\Delta N^2 \tau}{1 + 4\pi^2 f^2 \tau^2}} \tag{S7}$$

where ΔN^2 the mean square fluctuation of the number of carriers occupying the generation-recombination energy level. $\tau = (1/\tau_1 + 1/\tau_0)^{-1}$ represents the characteristic time constant related to the temperature, where τ_1 and τ_0 denote the lifetimes of a electron in the conduction band and trap level, respectively.

S6 Optical characteristics of CQD-based coupled heterostructures
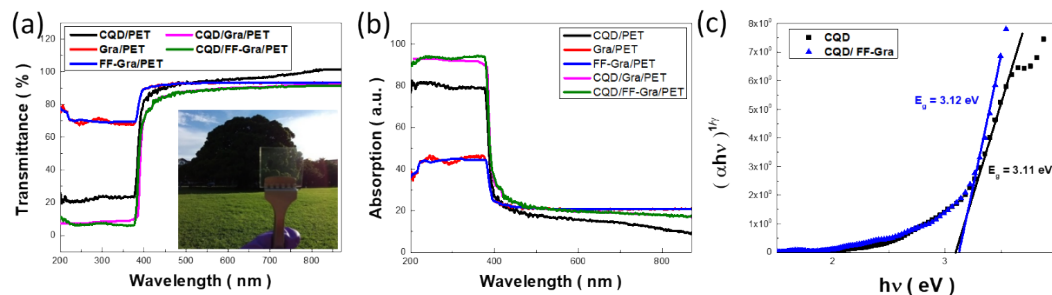## S6-1 Optical transmittance and absorption measurement

Fig. S6 The optical (a) transmittance and (b) absorption of CQD/PET, Gra/PET, FF-Gra/PET, CQD/Gra/PET and CQD/FF-Gra/PET. Inset: The photograph of highly

transparent CQD/FF-Gra/PET flexible photodetector with area of 1.5x1.5 cm^2. (c) Tauc's plot of CQD and CQD/FF-Gra were calculated by absorption data.

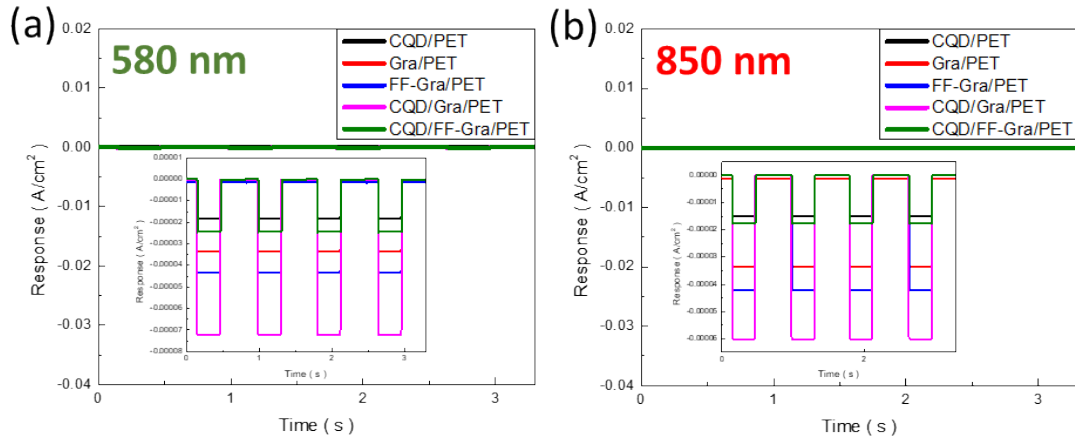## S7 Device characteristics: On-off switch photodetection

Fig. S7 On-off switching photoresponses under illuminated wavelength of (a) 580 nm and (b) 850 nm and their repetitive on/off cycles are recorded. The results show that the photocurrent values of CQD/PET, Gra/PET, FF-Gra/PET, CQD/Gra/PET and CQD/FF-Gra/PET devices under two different illuminated light wavelengths (580 nm/850 nm) are 36.7/35.4 nA/cm^2, 5.1/4.6 nA/cm^2, 6.2/5.67 nA/cm^2, 57.3/4.7 nA/cm^2 and 44.3/5.0 nA/cm^2, respectively.

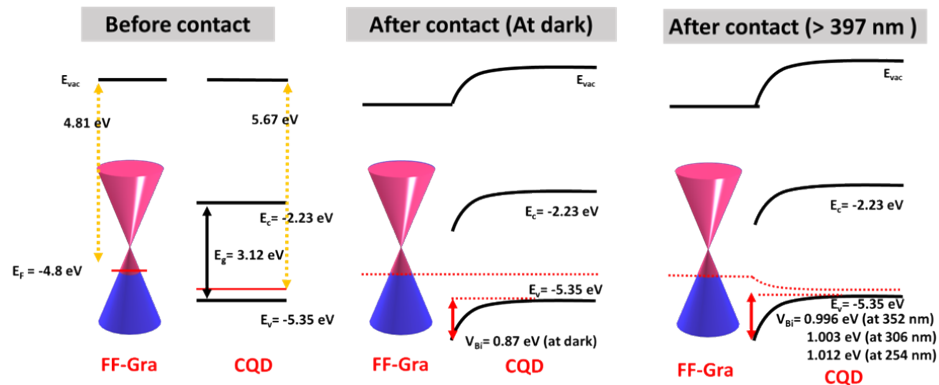## S8 Band structures of CQD/FF-Gra/PET

Fig. S8 Energy diagrams of the CQD/FF-Gra before contact, in the dark and under the illumination of UV lights under the bias of 0 V.

S9 PLQY examinations and carrier dynamics

Photoluminescence quantum yield (PLQY) results of CQD, CQD/Gra and CQD/FF-Gra samples are extracted from PL results, and the correlated radiative decay rates are given by the following equation:

$$Kr(Radiative\ decay\ rate) = \frac{PLQY}{Lifetime} \tag{S8}$$

Accordingly, the correlated PLQY and detailed results of carreir dynamics from different samples are summarized in Tables S4 and S5, respectively.

Table S4 Calculated PLQY of CQD, CQD/Gra and CQD/FF-Gra.

Sample	$PLQY_{total}$	$PLQY_{Exciton}$	$PLQY_{trion}$
CQD	0.33	0.064	0.155
CQD/Gra	0.30	0.071	0.17
CQD/FF-Gra	0.4	0.049	0.267

Table S5 Transient examinations of excited-state absorption (ESA) and stimulated emission of both bare CQD and CQD/FF-Gra structures, where the lifetimes of bound-carrier growth and recovery are monitored at 425 nm and 575 nm of two probing wavelengths, respectively.

Sample	Probe wavelength (nm)	Growth	Recovery		
		τ	τ_1	τ_2	τ_3
CQD	425	0.56 ps	0.24 ps (~ 91.3 %)	1.93 ps (~8.7 %)	N/A
	575	1.48 ps	4.2 ps (100 %)	N/A	N/A
CQD/FF-Gra	425	0.58 ps	0.68 ps (~ 58 %)	1.76 ps (~42 %)	N/A
	575	$\tau_1 = 1.42$ ps $\tau_2 = 0.93$ ps	11.4 ps (100 %)	N/A	N/A
	575	$\tau_1 = 1.42$ ps $\tau_2 = 0.93$ ps	8.72 ps (~72 %)	4.41 ps (~28%)	N/A

S10 Practical mechanical stability of the flexible transparent photodetectors
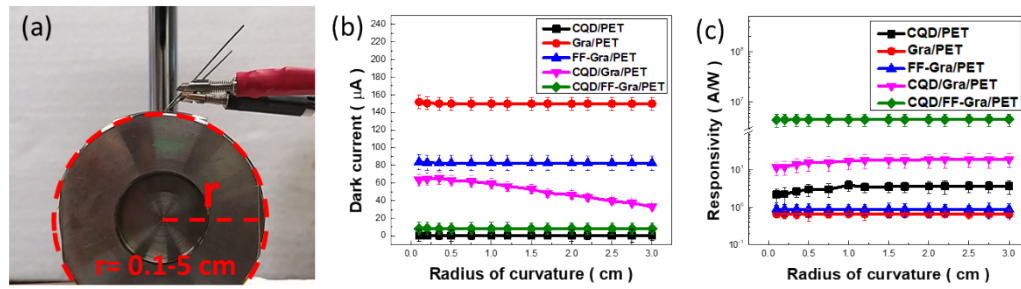## S10-1 Testing configuration and LBIC mapping after the bending test

Fig. S9 (a) Photograph of home-made measured system. The spectral (b) dark current and (c) responsivity of CQD/PET, Gra/PET, FF-Gra/PET, CQD/Gra/PET and CQD/FF-Gra/PET devices as a function of curvature radius after 120 times bending.

To investigate the mechanical stability of the flexible transparent photodetectors, repeated bending test are performed as functions of the curvature radius (r) (r= 5-0.1 cm), as shown in Fig. S9(a). The resulting dark currents of Gra/PET, FF-Gra and CQD/FF-Gra/PET are almost invariant under all the bending deformations at r= 0.1 cm of bending condition, respectively, as shown in Fig. S9(b). Nevertheless, both samples of CQD/PET and CQD/Gra/PET exhibit the unstable performances and feature the large variation of dark currents by 38% and 48.2 % after the 120 cycles bending test at r= 0.1 cm, respectively. In addition, the responsivity results of Gra/PET, FF-Gra/PET and CQD/FF-Gra/PET are almost consistent under the bending deformations, as evidenced in Fig. S9(c).
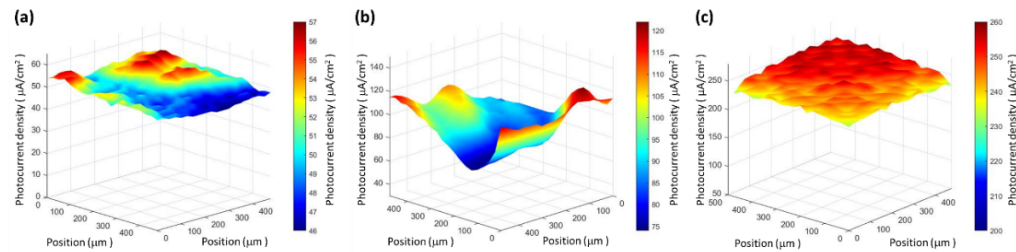

Fig. S10 Laser beam induced current (LBIC) measurement of (a) CQD/PET, (b) CQD/Gra/PET and (c) CQD/FF-Gra/PET after the bending test (120 cycles) at r = 0.5 cm.

The bending tests are employed at a bending frequency of 1 Hz under an area of 400 μm×400 μm. In the case of CQD/FF-Gra/PET, the mapping results display the uniform distribution of photocurrents after the bending test with a small standard deviation of 1.82 %, as evidenced in Fig. S10(c). By contrast, CQD/PET and CQD/Gra/PET showed the relatively uneven results after undergoing bending test, with large standard deviation of 11.43 % [Fig. S10(a)] and 27.72 % [Fig. S10(b)], respectively.

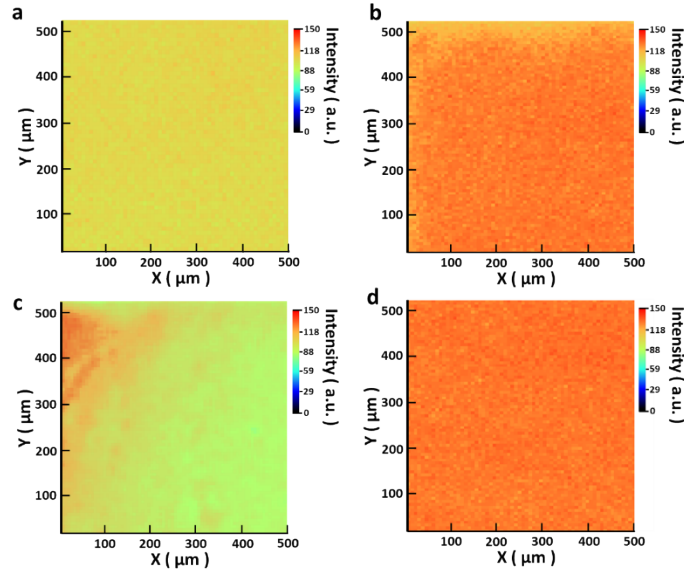## S10-2 PL mapping after the bending test

Fig. S11 Spatial photoluminescence mapping of (a)CQD/Gra/PET, (b)CQD/FF-Gra/PET before and (c)(d) after bending test.
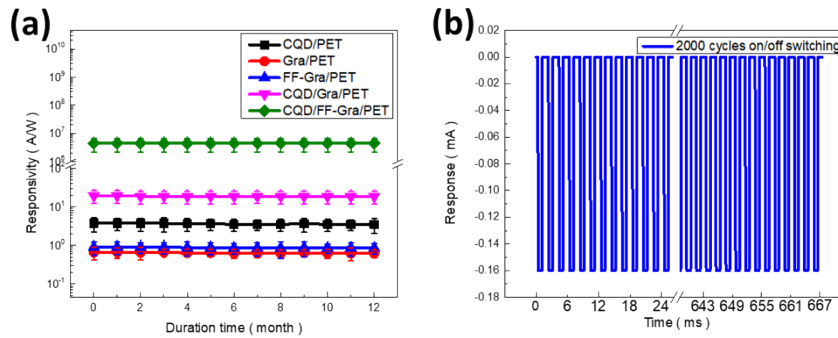
S10-3 Cycling reliability

Fig. S12 (a) Long-term duration test of CQD/PET, Gra/PET, FF-Gra/PET, CQD/Gra/PET and CQD/FF-Gra/PET devices, respectively. (b)On/off cycling test of CQD/FF-Gra/PET. The long-term duration test (12 months) of CQD/PET, Gra/PET, FF-Gra/PET, CQD/Gra/PET and CQD/FF-Gra/PET devices reveal that the correlated decrease of responsivities are found to be 12.3%, 0.88 %, 0.93%, 6.5 % and 0.72 % after 12-month duration, respectively, as shown in Fig. S12(a). In addition, the extremely low reduction of photoresponse (~0.4%) in the case of CQD/FF-Gra/PET around 0.4 % is featured under 2000-cycle examinations, as demonstrated in Fig. S12(b).

S11 Performance comparison of transparent flexible photodetectors
Table S6 Summary of comparative photodetection performances from transparent flexible photodetector devices

Sample	R (A/W)	D (Jones)	Bias (V)	Reference
n-SnO$_2$-p-ZnO:Ag	8.67 A/W	2.33×10^{13} Jones	5 V	[1]

a-IGZO MSM	5 mA/W	5.1×10^{12} Jones	-0.5 V	2
ITO/SWCNT/ITO	1.02×10^{4} A/W	1.73×10^{16} Jones	10 V	3
β-Ga$_2$O$_3$/γ-In$_2$O$_3$/α-Al$_2$O$_3$	94.3 A/W	3.09×10^{12} Jones	-5 V	4
ITO/TAPC: C$_{60}$/Al	2.91×10^{3} A/W	1.28×10^{14} Jones	-14 V	5
Graphite QDs/graphene	2.3×10^{6} A/W	5.5×10^{13} Jones	1 V	6
AgNW@ZnO NRs	6.5×10^{-6} A/W	1.15×10^{10} Jones	5 V	7
n-ZnO/n-V2O5	18.9 A/W	10^{12} Jones	-4 V	8
WS2-QDs/RGO	5.22×10^{-3} A/W	1.6×10^{6} Jones	12 V	9
β-Ga2O3:Si MESFET	74.0 A/W	2.2×10^{14} Jones	5 V	10
CQD/FF-Gra	**4.7X10^{6} A/W**	**2.7X10^{17} Jones**	**1 V**	**This work**

REFERENCE
1. Z. Long, X. Xu, W. Yang, M. Hu, D. V. Shtansky, D. Golberg and X. Fang, *Adv. Electron. Mater.*, 2020, **6**, 1901048.

2. C.-Y. Huang, T.-Y. Peng and W.-T. Hsieh, *ACS Appl. Electron. Mater.*, 2020, **2**, 2976-2983.

3. Y. Zhou, J. Chen, R. Yu, E. Li, Y. Yan, J. Huang, S. Wu, H. Chen and T. Guo, *J. Mater. Chem. C*, 2021, **9**, 1604-1613.

4. K.-H. Li, C. H. Kang, J.-H. Min, N. Alfaraj, J.-W. Liang, L. Braic, Z. Guo, M. N. Hedhili, T. K. Ng and B. S. Ooi, *ACS Appl. Mater. Interfaces*, 2020, **12**, 53932-53941.

5. D. Guo, L. Yang, J. Zhao, J. Li, G. He, D. Yang, L. Wang, A. Vadim and D. Ma, *Mater. Horizons*, 2021, **8**, 2293-2302.

6. H. Tetsuka, A. Nagoya and S.-i. Tamura, *Nanoscale*, 2016, **8**, 19677-19683.

7. L. Zhang, N. Li, Q. Ma, J. Ding, C. Chen, Z. Hu, W. Zhao, Y. Li, H. Feng and M. Li, *J. Mater. Sci. Technol.*, 2022, **110**, 65-72.

8. N. Kumar, T. T. Nguyen, M. Patel, S. Kim and J. Kim, *J. Alloys Compd.*, 2022, **898**, 162788.

9. Abid, P. Sehrawat, C. Julien and S. Islam, *ACS Appl. Mater. Interfaces*, 2020, **12**, 39730-39744.

10. Z. Liu, M. Zhang, L. Yang, S. Li, S. Zhang, K. Li, P. Li, Y. Guo and W. Tang, *Semicond. Sci. Technol.*, 2021, **37**, 015001.